This is the accepted manuscript made available via CHORUS. The article has been published as:

Nonequilibrium steady-state thermoelectrics of Kondo-correlated quantum dots

Anand Manaparambil, Andreas Weichselbaum, Jan von Delft, and Ireneusz Weymann

Phys. Rev. B **111**, 035445 — Published 27 January 2025

DOI: 10.1103/PhysRevB.111.035445

Nonequilibrium steady-state thermoelectrics of Kondo-correlated quantum dots

Anand Manaparambil,[1,*] Andreas Weichselbaum,[2] Jan von Delft,[3] and Ireneusz Weymann[1]

[1] *Institute of Spintronics and Quantum Information, Faculty of Physics, Adam Mickiewicz University, Uniwersytetu Poznańskiego 2, 61-614 Poznań, Poland*

[2] *Department of Condensed Matter Physics and Materials Science, Brookhaven National Laboratory, Upton, New York 11973-5000, USA*

[3] *Arnold Sommerfeld Center for Theoretical Physics, Center for NanoScience, and Munich Center for Quantum Science and Technology, Ludwig-Maximilians-Universität München, 80333 Munich, Germany*

(Dated: January 3, 2025)

The transport across a Kondo-correlated quantum dot coupled to two leads with independent temperatures and chemical potentials is studied using a controlled non-perturbative, and in this sense numerically exact treatment based on a hybrid numerical renormalization group combined with time-dependent density matrix renormalization group (NRG-tDMRG). In the Kondo regime for sufficiently large fixed voltage bias $V \gtrsim T_K$ with T_K the Kondo temperature, we find a peak in the conductance vs. the temperature gradient $\Delta T = T_R - T_L$ across left and right lead. Focusing then on zero voltage bias but finite ΔT far beyond linear response, we reveal the dependence of the characteristic zero-bias conductance on the individual lead temperatures. We find that the finite-ΔT data behaves quantitatively similar to linear response with an effective equilibrium temperature derived from the different lead temperatures. The regime of sign changes in the Seebeck coefficient, signaling the presence of Kondo correlations, and its dependence on the individual lead temperatures provide a complete picture of the Kondo regime in the presence of finite temperature gradients. The results from the zero-bias conductance and Seebeck coefficient studies unveil an approximate 'Kondo circle' in the T_L/T_R plane as the regime within which the Kondo correlations dominate. We also study the heat current and the corresponding heat conductance vs. finite ΔT. We provide a polynomial fit for our numerical results for the thermocurrent as a function of the individual lead temperatures which may be used to fit experimental data in the Kondo regime.

I. INTRODUCTION

Strong electronic correlations in a magnetic impurity coupled to electronic reservoirs result in a many-body screening phenomenon, mediated by the conduction band electrons, known as the Kondo effect [1]. The Kondo effect manifests itself in the density of states of the impurity as a narrow resonance peak around the Fermi level widely known as the Kondo-Abrikosov-Suhl resonance [2, 3]. This Kondo resonance that increases the low temperature resistivity of bulk metal alloys [4] has been found to be present in various classes of nanostructures, involving single electron transistors [5–10], nanowires [11–14], carbon nanotubes [15, 16], molecular magnets [17–19], adatoms [20–22] and other quantum impurity systems [23–27]. Such nanostructures are very tunable and act as a robust platform to explore various aspects of the Kondo effect [6, 28]. Moreover, the transport properties of Kondo-correlated impurity systems carry characteristic signatures of the Kondo effect, which emerge at low temperatures near the Kondo energy scale. Particularly, the zero-bias peak in the differential conductance [5, 6] and a sign change in the Seebeck coefficient at low energies [29–33] signify the presence of Kondo correlations in the system. The characteristic density of states present in the quantum dots makes them a class of prospective systems to work as efficient energy-harvesters [34–42]. Various proposals, such as the charge Kondo effect [43], multi-quantum dot setups [44, 45], including the case of asymmetric couplings to the leads [46, 47], have pointed towards a considerable thermoelectric efficiency of quantum-dot based heat engines. Thermoelectric quantum dot devices have also demonstrated promising applications in sensing [46, 48] and cooling technologies [49–51].

An accurate description of the Kondo effect relies on the exact treatment of electronic correlations at low energy scales. Though many theoretical methods, including the Bethe-Ansatz [52, 53], perturbation theory [54], Fermi liquid theory [55] and the dynamical mean field theory [56], can tackle the Kondo problem and contribute to the qualitative understanding of the phenomenon at low energies, all of them rely on approximating the electronic correlations to describe the energies near the Kondo energy scale. The numerical renormalization group method (NRG) [57, 58], considered to be the best at tackling the Kondo problem, can provide quantitatively accurate description of the Kondo effect, but only up to linear response studies near equilibrium [29].

A multitude of other theoretical approaches to tackle nonequilibrium transport through Kondo-correlated quantum dots have been reported in the literature. A far-from-complete listing includes works based on nonequi-

* anaman@amu.edu.pl

librium Greens function (NEGF) [59–61], renormalized perturbation theory (RPT) [62], generalized Fermi liquid theory [63–66], perturbative approaches [47, 67], auxiliary master equation approach (AMEA) [48, 68, 69], noncrossing approximation (NCA) [70, 71], functional renormalization group method (fRG) [72–74], real-time density matrix renormalization group method (tDMRG) [73, 75], quantum Monte Carlo techniques (QMC) [73, 76–78], iterative summation of real-time path integrals (ISPI) [73, 79], or slave-boson mean field theory (SBMFT) [60]. Though each method has its own virtues and provides theoretical insights at various limits, a complete picture of the whole nonequilibrium Kondo regime had remained elusive. A hybrid method, incorporating both numerical renormalization group and time-dependent density matrix renormalization group (tDMRG) method based on a thermofield quench approach (NRG-tDMRG), has achieved the feat of describing the nonequilibrium transport through a Kondo-correlated system with exact treatment of correlations [80]. Until now, this method has been employed to address the electronic transport under finite potential bias [80] and spintronic transport in the presence of ferromagnetism in the leads [81]. In this work, we extend the NRG-tDMRG method to describe the nonequilibirum Kondo effect in the presence of finite temperature gradients. In particular, we consider a quantum dot symmetrically coupled to two metallic leads held at different temperatures that can be tuned independently. The choice of symmetric couplings to the leads allows for the Kondo correlations to develop over both the leads, uncovering the influence of the individual lead temperatures on the Kondo effect. The dynamics of the electronic and heat currents are calculated using NRG-tDMRG and their nonequilibrium steady state values are extracted using linear prediction across a finite time window. We characterize the Kondo regime as a function of the individual lead temperatures using the zero-bias conductance and the Seebeck coefficient of the system. We find that transport in the presence of a nonlinear temperature gradient can be qualitatively described by linear response results with an effective equilibrium temperature. Our results demonstrate that the Kondo correlations persist as a circle when depicted in the individual lead temperatures.

Our work provides quantitatively accurate results for the thermoelectric transport coefficients of Kondo-correlated quantum dot in far-from-equilibrium settings. The paper is organized as follows: Sec. II describes the system Hamiltonian and the transport properties under study. In Sec. III, we discuss the results from NRG-tDMRG calculations. We begin by discussing a noninteracting system in Sec. III A, and then moving on to the interacting system described by the single impurity Anderson model in Sec. III B. The influence of temperature gradient on the zero-bias transport properties is discussed in Sec. III B 1. The differential conductance at zero-bias and for a finite potential bias in the presence of different lead temperatures is discussed in Sec. III B 2. The thermoelectric current, Seebeck coefficient and heat transport properties are discussed in Sec. III B 3. Finally, the paper is summarized in Sec. IV.

II. MODEL AND METHOD

A. Hamiltonian

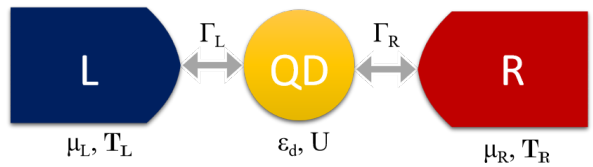

FIG. 1. The schematic of a quantum dot with orbital level ε_d and Coulomb repulsion U coupled to the left ($\alpha = L$) and right ($\alpha = R$) metallic lead with hybridization function Γ_α. Each lead is held at different temperature T_α and chemical potential $\mu_\alpha = \pm V/2$.

Our system consists of a quantum dot strongly coupled to two metallic leads. The Hamiltonian of such a system can be described as

$$H = H_{\rm imp} + H_{\rm lead} + H_{\rm tun}, \tag{1}$$

where $H_{\rm imp}$ is the impurity part of the Hamiltonian described by a single impurity Anderson model (SIAM) with orbital energy ε_d and Coulomb interaction U. $H_{\rm imp}$ takes the form

$$H_{\rm imp} = \varepsilon_d(n_\uparrow + n_\downarrow) + U\, n_\uparrow n_\downarrow, \tag{2}$$

where $n_\sigma = d^\dagger_\sigma d_\sigma$ is the number operator, with $d_\sigma(d^\dagger_\sigma)$ being the annihilation (creation) operator for a dot electron with spin σ. The leads are modeled as noninteracting particles

$$H_{\rm lead} = \sum_\alpha H_\alpha = \sum_{\alpha k\sigma} \varepsilon_{\alpha k} c^\dagger_{\alpha k\sigma} c_{\alpha k\sigma}, \tag{3}$$

with $c_{\alpha k\sigma}$ ($c^\dagger_{\alpha k\sigma}$) denoting the annihilation (creation) operator for an electron in the lead α with energy $\varepsilon_{\alpha k}$ and spin σ. Finally, the tunneling Hamiltonian $H_{\rm tun}$ describes the coupling of the quantum dot to the leads

$$H_{\rm tun} = \sum_{\alpha k\sigma} (v_{\alpha k} d^\dagger_\sigma c_{\alpha k\sigma} + {\rm H.c.}), \tag{4}$$

where $v_{\alpha k}$ is the tunneling matrix element between the kth mode in the lead α and the quantum dot. The dot hybridizes with the leads with the coupling strength given by, $\Gamma_\alpha = \pi\rho_\alpha |v_{\alpha k}|^2$, where ρ_α denotes the density of states of the lead α, which is assumed to be flat $\rho_\alpha \equiv 1/2D$, with D being the band halfwidth which is used as the unit of energy, hence $D = 1$. In the following, without loss of generality, we assume that the system is symmetric $\Gamma_L = \Gamma_R = \Gamma$. We set

$$\Gamma = 0.001, \quad U = 12\,\Gamma, \quad \varepsilon_d = -U/3, \tag{5}$$

unless specified otherwise. The bias voltage V is applied symmetrically as $\mu_L = -\mu_R = V/2$ and the left and right lead temperatures T_L, T_R can be controlled independently.

To accurately take into account correlation effects at truly nonequilibrium settings, we employ a hybrid NRG-tDMRG method in the matrix product state (MPS) framework [80, 81] discussed in more detail in App. A . This method consists of a logarithmic-linear discretization scheme of the conduction bands, a thermofield treatment, followed by a recombination of the leads modes, and finally the time evolution by the second-order Trotter decomposition to reach the nonequilibrium steady-state. The steady state values as $t \to \infty$ of heat and charge currents are found from linear prediction of finite time dynamics (cf. App. B).

The hybrid NRG-tDMRG approach includes strictly linear discretization within the *dynamical* or *transport window*, with the time evolution carried out in this discretized basis by tDMRG.The uniform linear discretization in the transport window is essential for an unbiased approach to out-of-equilibrium where any local excitations or transitions around the impurity are energetically allowed, driven by the voltage or temperature differences across the leads [80, 81]. By focusing on out-of-equilibrium with $\max(V, \Delta T) \gtrsim T_K$ we thus uncover the transport behavior in the Kondo scaling regime far beyond linear response.

The energy resolution of our method is set by the linear level spacing in the transport window. To be specific, this sets the resolution of the smallest energy scale $\min(T_L, T_R)$ relative to the largest energy scale $\max(V, T_L, T_R)$, In our calculations we keep $N_L = 100$ linearly discretized levels inside the transport window which sets the linear discretization parameter, i.e., the level spacing $\delta \sim \max(V, T_L, T_R)/N_L$ [cf. App. A]. Therefore we need to maintain $\min(T_L, T_R) \gtrsim \delta$ to avoid discretization artifacts, in the sense that temperature smears out the discrete level spacing, specifically so when taking gradients w.r.t. temperature. Assuming that there are no spectral features in the dynamical window that are narrower than the level spacing δ, however, this is no actual physical constraint, but rather a computational aspect to bear in mind. For calculations with a finite thermal bias, our choice of N_L thus sets an upper limit on the difference in the temperatures of the left vs. right lead to around two orders of magnitude. The numerical cost of one tDMRG sweep is of the order of $O(Lm^3)$, where $L \sim 4N_L$ the system size and m the bond dimension of the underlying MPS .

B. Transport coefficients

The charge current $J_{\alpha\sigma}$ from the lead α to the quantum dot in the spin channel σ is given by

$$\begin{aligned} J_{\alpha\sigma} &= e\,\langle \dot{N}_{\alpha\sigma}\rangle = -\tfrac{ie}{\hbar}\langle [N_{\alpha\sigma}, H]\rangle \\ &= \tfrac{e}{\hbar}\sum_k \mathrm{Im}\,(v_{\alpha k}\,\langle d^\dagger_\sigma c_{\alpha k\sigma}\rangle). \end{aligned} \tag{6}$$

Here, $N_{\alpha\sigma} = \sum_k c^\dagger_{\alpha k\sigma} c_{\alpha k\sigma}$ is the occupation number in the lead α. Similarly, the energy current J^E_α from the lead α to the quantum dot can be described based on the lead Hamiltonian H_α as

$$\begin{aligned} J^E_\alpha &= \langle \dot{H}_\alpha\rangle = -\tfrac{i}{\hbar}\langle [H_\alpha, H]\rangle \\ &= \tfrac{1}{\hbar}\sum_{k\sigma} \varepsilon_{\alpha k}\,\mathrm{Im}\,(v_{\alpha k}\,\langle d^\dagger_\sigma c_{\alpha k\sigma}\rangle). \end{aligned} \tag{7}$$

In the case of $V = 0$, the energy current can be considered as the heat current $J^Q \equiv J^E$. We note that since the symmetrized charge (heat) current $J^{(Q)}(t)$ converges faster than the current contributions from the individual leads, $J^{(Q)}_{\alpha\sigma}(t)$, it is more efficient to find the steady-state value of the total current $J^{(Q)}(t)$,

$$J^{(Q)}(t) = \sum_\sigma \tfrac{1}{2}[J^{(Q)}_{L\sigma}(t) - J^{(Q)}_{R\sigma}(t)]. \tag{8}$$

More details about estimating $J^{(Q)}(t)$ and the steady state $J^{(Q)}$ can be found in App. B.

The differential electronic conductance G and the electronic contribution to the heat conductance κ are respectively defined as

$$\begin{aligned} G &= \left(\frac{dJ}{dV}\right)_{T_L,\,T_R}, \\ \kappa &= \left(\frac{J^Q}{\Delta T}\right)_V. \end{aligned} \tag{9}$$

The Seebeck coefficient S estimates the potential V required to compensate for the induced thermoelectric current J under a finite temperature gradient ΔT and it is defined as

$$S = -\left(\frac{V}{\Delta T}\right)_{J=0}. \tag{10}$$

For the transport across an impurity coupled to metallic leads in the linear response regime, these transport coefficients can be estimated as a function of the Onsager integrals, $L_n = -\frac{1}{h}\int d\omega(\omega-\mu)^n \frac{\partial f}{\partial \omega}\mathcal{T}(\omega)$, where $\mathcal{T}(\omega)$ is the transmission coefficient of the impurity and it is essentially equivalent to the equilibrium spectral function $A(\omega)$ [82]. The linear response transport coefficients can thus take the form [29]

$$\begin{aligned} G_0 &= e^2\,L_0, \\ S_0 &= -\tfrac{1}{eT}\tfrac{L_1}{L_0}, \\ \kappa_0 &= \tfrac{1}{T}\left(L_2 - \tfrac{L_1^2}{L_0}\right). \end{aligned} \tag{11}$$

III. RESULTS AND DISCUSSION

In this section, we present and discuss the NRG-tDMRG results for the nonequilibrium transport through a quantum dot in the presence of temperature gradients. First we benchmark our method against analytical results for the non-interacting case in Sec. III A. While focusing predominantly on finite temperature difference at infinitesimal voltage bias for the interacting case in Sec. III B then, we nevertheless also uncover a peak in the conductance vs. temperature gradient ΔT in the Kondo regime for sufficiently large fixed voltage bias $V \gtrsim T_K$ in Fig. 5(c). The details of the NRG-tDMRG calculations are described in App. A where the method specific parameters are provided in App. A 4.

A. Noninteracting case: Resonant Level Model

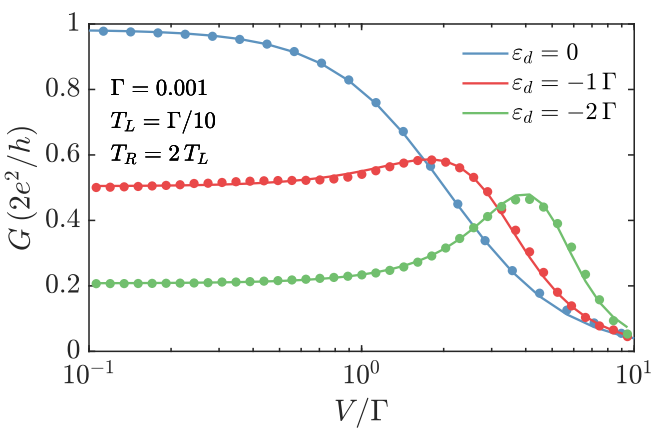

FIG. 2. The differential conductance for the resonant level model ($U = 0$) vs. potential bias V for fixed $\Delta T \sim T$ (see model parameters to the left) and orbital energies ε_d as indicated in the legend. NRG-tDMRG data (dots) is compared to exact analytic curves for continuum (lines) as a consistency check.

As a benchmark for the nonequilibrium calculations, we consider the noninteracting resonant level model (RLM), i.e., essentially the Anderson model with $U = 0$. For this case, the current flowing through the system can be solved exactly [82]

$$J(V, \Delta T) = \frac{2e}{h} \int d\omega\, \mathcal{T}(\omega)\, [f_L(\omega) - f_R(\omega)], \qquad (12)$$

where $\mathcal{T}(\omega)$ denotes the transmission coefficient, which can be related to the quantum dot spectral function $A(\omega)$, $\mathcal{T}(\omega) = \pi\Gamma A(\omega)$. For the noninteracting quantum dot, the spectral function can be found exactly through the equation of motion for the Green's function. The transmission coefficient is then given by $\mathcal{T}(\omega) = \Gamma^2/(\Gamma^2 + (\omega - \varepsilon_d)^2)$, where $f_\alpha(\omega) = 1/\{1 + \exp[(\omega - \mu_\alpha)]/T_\alpha\}$ is the Fermi-Dirac distribution function of lead α with $k_B \equiv 1$. The differential conductance $G(V)$ calculated using NRG-tDMRG method for a noninteracting quantum dot with different orbital level energies ε_d in the presence of finite potential and temperature gradients is shown in Fig. 2. The differential conductance $G(V)$ has a peak around $V = 2\,\varepsilon_d$, which is attributed to the Lorentzian peak in $A(\omega)$ located at $\omega = \varepsilon_d$. The shift in the differential conductance peak from the Lorentzian peak originates from the symmetric nature of applied bias $\mu_L = -\mu_R = V/2$, resulting in the transport window (TW) $[f_L(\omega) - f_R(\omega)]$ inside the integral in Eq. (12) scanning the peak mainly around $\omega = 2\,V$. It is important to note that both temperatures (T_L, T_R) smear out the transport window and can thus only broaden the conductance peak. Our NRG-tDMRG data in Fig. 2 (dots) which necessarily operates in the discretized setting agrees well with the exact analytical calculations without any discretization, i.e., in the continuum limit (lines). This demonstrates that our technique can capture the nonequilibrium transport primarily originating from the nonlinear dependence of the lead Fermi distributions on V and T.

B. Interacting case: Single Impurity Anderson Model

In the presence of finite U, the nonequilibrium transport across the quantum dot becomes highly nontrivial and cannot be boiled down to an analytical description without sufficient approximations [60, 65]. But, the linear response description of transport across an interacting quantum dot in equilibrium can very well be calculated using the definitions in Eq. (12) once the spectral function $A(\omega)$ is obtained. The equilibrium spectral function $A(\omega)$ of a SIAM with finite U can be calculated using NRG with extreme precision, and thus it will be used as the benchmark for the calculation of linear response coefficients. The NRG data discussed in this section have been calculated using the QSpace tensor library for Matlab [83–85] with discretization parameter $\Lambda = 2$, iteration number $N = 60$ and the maximum number of states kept $N_{\rm K}$ after each iteration as 2^{10}.

1. *Influence of finite temperature gradient*

We first introduce the finite temperature gradient across a SIAM by keeping the left lead temperature at $T_L = 0.01\Gamma$ and changing the right lead temperature from $T_R = 0.01\Gamma$ to $T_R = 0.5\Gamma$. The electric current $J(V, T_L, T_R)$ and heat current $J^Q(V, T_L, T_R)$ across the SIAM using (5) is calculated for bias voltages close to linear response $V_0 \approx 0.005\,\Gamma$ using the NRG-tDMRG method. Thus the differential conductance $G(T_L, T_R) \equiv G(V = 0, T_L, T_R)$ can be estimated as

$$G(T_L, T_R) = \tfrac{1}{2V_0}\Big(J(V_0) - J(-V_0)\Big)\Big|_{T_L, T_R}. \qquad (13)$$

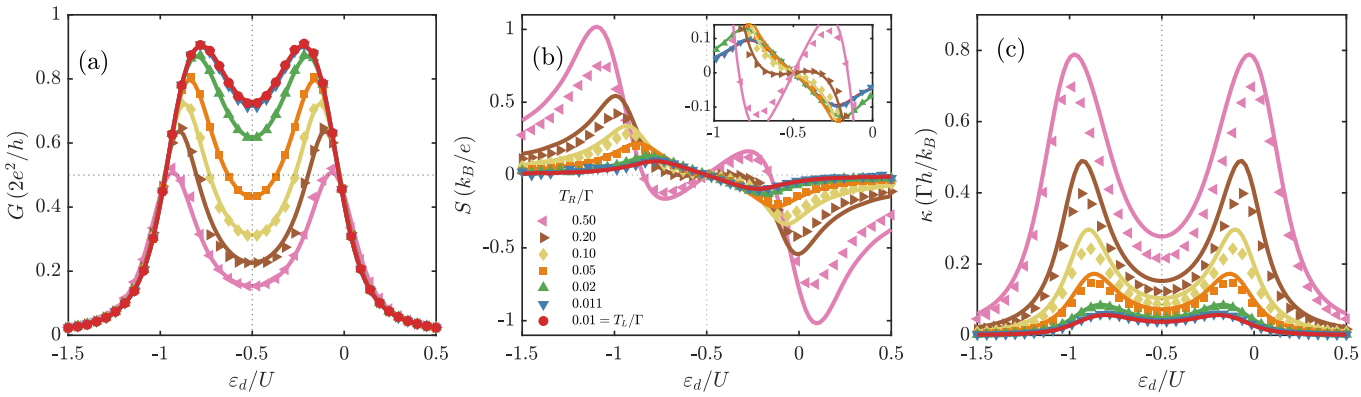

FIG. 3. (a) Differential conductance G, (b) Seebeck coefficient S, and (c) heat conductance κ of an interacting quantum dot [SIAM using parameters (5) except for ε_d which is varied here] vs. orbital level position ε_d in the linear response regime with respect to the bias voltage. The left lead is kept at temperature $T_L = 0.01\,\Gamma$ throughout, while the right lead temperatures are specified with the legend in (b). The colored symbols are the nonequilibrium data from the NRG-tDMRG calculations and the solid lines present the equilibrium NRG data with the same parameters but calculated for an effective global temperature $T_{\rm eff} = T_{\rm rms}$. Numerically, the determination of S and κ require a finite temperature difference ΔT. Hence, no red dots are shown for the case $T_L = T_R$ in (b) and (c). The limiting case $\Delta T \to 0$, however, is reflected in the small $\Delta T/T \sim 0.1$ data set (blue triangles), which already agrees well with the equilibrium NRG data for $\Delta T = 0$ (red line).

The choice of linear response bias voltage V_0 is such that any nonlinear behavior of $G(V)$ can be avoided, allowing us to treat the estimated currents as linear in V. Since the bias values $V = \pm V_0$ are effectively in the linear response regime, the charge (heat) current $J^{(Q)}$ at zero bias can be calculated according to the linear response expansion as,

$$J^{(Q)}(T_L, T_R) = \tfrac{1}{2}\Big(J^{(Q)}(V_0) + J^{(Q)}(-V_0)\Big)\Big|_{T_L,T_R}. \quad (14)$$

The electronic contribution to the heat conductance according to Eq. (9) can thus be $\kappa(T_L, T_R) = J^Q(T_L, T_R)/(T_R - T_L)$. The information about $J(T_L, T_R)$ and $G(T_L, T_R)$ at $V = 0$ is sufficient to calculate the Seebeck coefficient S for the respective parameters. Moreover, the linear response in V allows the current for small voltages to be expressed as $J(V) = J(0) + V\,G$ for constant T_L and T_R. Thus the Seebeck coefficient S from its definition in Eq. (10) can be estimated as,

$$S(T_L, T_R) = -\frac{1}{T_R - T_L}\frac{J(T_L, T_R)_{V=0}}{G(T_L, T_R)_{V=0}}. \quad (15)$$

The transport coefficients for a quantum dot in the presence of finite temperature gradient calculated using NRG-tDMRG are shown in Fig. 3. The differential conductance G seen in Fig. 3(a) shows the evolution of the zero-bias conductance peak as a function of the orbital energy ε_d. The red dots in Fig. 3(a) display the NRG-tDMRG data for $T_L = T_R = 0.01\,\Gamma$, which match exactly with the equilibrium NRG data (red curve) for G_0 computed with a global temperature $T = 0.01\Gamma$. The large conductance inside the local moment regime, $-U \lesssim \varepsilon_d \lesssim 0$, is a characteristic feature of the Kondo resonance and the thermal fluctuations from the leads with temperature $T = 0.01\,\Gamma$ limit the conductance from reaching the unitary value of $G_0 = 2e^2/h$.

The Kondo temperature $T_{\rm K}$ in the local moment regime is analytically given by the improved Haldane formula from Fermi liquid theory [64]

$$T_{\rm K} = \sqrt{\frac{\Gamma\,U}{2}}\exp\left[\frac{\pi\,\varepsilon_d\,(\varepsilon_d + U)}{2\,\Gamma\,U} + \frac{\pi\,\Gamma}{2\,U}\right]. \quad (16)$$

Since the Kondo temperature represents a crossover scale, it is only defined up to a prefactor of order one. Hence, alternatively from a data or experimental point of view, the Kondo temperature can be estimated by the temperature at which the zero-bias conductance drops by half. Below, we will refer to this as $T_{K'}$, where based on our data for the parameters in Eq. (5), $T_{\rm K'} \simeq 1.05\,T_{\rm K}$ [cf. Fig. 4(c) and caption].

For the SIAM parameters in Eq. (5), we have $T_{\rm K} = 0.042\,\Gamma$ [as compared to the lowest value at $\varepsilon_d = -U/2$, $T_{\rm K} = 0.025\,\Gamma$]. Thus, in the local moment regime, the $G(\varepsilon_d)$ curves in Fig. 3(a) show minima at $\varepsilon_d = -U/2$ corresponding to the lowest $T_{\rm K}$. We proceed to heat up the right lead (T_R), as specified in the legends of Fig. 3. With increasing T_R, the differential conductance in the local moment regime decreases as the Kondo resonance dies off with increasing thermal fluctuations from the hotter lead. The equilibrium NRG cannot account for different lead temperatures, but one can still define an effective global temperature $T_{\rm eff}$ at equilibrium as the root mean square value of the left and right lead temperatures

$$T_{\rm eff} = T_{\rm rms} = \sqrt{\tfrac{1}{2}(T_L^2 + T_R^2)}. \quad (17)$$

The significance of the root mean square value will be discussed in the next section, Sec. III B 2. For the sake of

the discussion here, it is sufficient to note that $T_{\rm rms} \to T$ when $T_R \to T_L$.

In Fig. 3 we show that a striking agreement exists between the nonequilibrium NRG-tDMRG results at finite thermal bias (colored symbols) and the equilibrium NRG results with an effective global temperature $T_{\rm rms}$ defined as the root mean square value of the lead temperatures. Implying that the dependence on the individual lead temperatures mimics the dependence of equilibrium Kondo resonance width with a global temperature $T_{\rm rms}$. This is consistent with the low temperature limit from the perturbation theory and slave-boson mean field theory results of Ref. [60]. Moreover, the NRG-tDMRG results are valid for higher temperatures due to the exact treatment of correlations. It is also interesting to note that this effective $T_{\rm rms}$ equivalence extends even into the mixed valence and empty/filled orbital regimes ($\varepsilon_d \lesssim -U, \varepsilon_d \gtrsim 0$). Furthermore, the experimental works for the thermoelectrics in the Kondo regime show a good agreement with our results. Figure 2 of Ref. [30], showing the differential conductance and thermocurrent with $\Delta T/T \approx 0.3$ for different T near the Kondo regime, behaves in a very similar way to the results presented here. On the other hand, the experimental data for the Seebeck coefficient shown in Fig. 4 of Ref. [31] were related to the linear response NRG results. We note that in this case, the corresponding temperature gradients, though not precisely determined due to the experimental conditions, reached $\Delta T/T \approx 2/3$ which is well beyond linear response theory. The qualitative agreement obtained with linear-response NRG, nevertheless, we attribute to the $T_{\rm rms}$ equivalence discussed in this paper. A more quantitative agreement can be obtained using $T = T_{\rm rms}$ in the NRG calculations, provided that the temperatures of the individual leads are known. Of course, deep in nonequilibrium, i.e., much beyond linear response, one needs to resort to out-of-equilibrium approaches such as NRG-tDMRG.

The linear response Seebeck coefficient S_0 of a quantum dot as a function of the global temperature has been shown to change sign with the onset of the Kondo correlations [29–31, 60]. On the other hand, the nonlinear temperature gradient dependence of S in the Kondo regime is largely unknown. Here, with our NRG-tDMRG method, we are able to provide reliable quantitative data as presented in Fig. 3(b). The red curve represents the equilibrium case where $T_{\rm rms} = T_L = T_R = 0.01\,\Gamma$. Note that the calculation of S from NRG-tDMRG requires a finite temperature gradient according to Eq. (15) and thus nonequilibrium data is absent for the $T_L = T_R$ case. The representative linear response results from NRG-tDMRG are presented in the case of $T_R = 0.011\,\Gamma$ (blue traingles) and agree well with the equilibrium results from NRG. The Seebeck coefficient remains antisymmetric across the particle-hole symmetry point $\varepsilon_d = -U/2$ and has a nonzero value in the local-moment regime, as expected for finite temperatures below $T_{\rm K}$.

When the right lead temperature is increased, i.e. with a finite thermal bias, the Seebeck coefficient becomes reduced and starts to change sign in the local moment regime around $T_R = 0.2\,\Gamma$, indicating the destruction of the Kondo resonance. Interestingly and quite unexpectedly, the comparison to the equilibrium NRG results with a global temperature $T_{\rm rms}$ gives a reasonably good agreement in the local moment regime. The sign change in equilibrium $S_0(T)$ occurs at higher temperatures than $T_{\rm K}$, which is also reflected in our finite ΔT results. However, outside the local moment regime, where the Kondo correlations do not emerge, the Seebeck coefficient increases in magnitude (no sign changes) with the increase in T_R and, correspondingly, with $T_{\rm rms}$. In this regime, the effective linear response results show growing deviations from the nonequilibrium results with increasing temperature gradient.

Finally, for the sake of completeness, we examine the heat conductance κ as a function of ε_d in Fig. 3(c). The heat conductance is dominated by the contribution associated with charge fluctuations, which are most active at resonances. As can be seen, κ generally has two peaks corresponding to the proximity of the resonant levels to the Fermi energy at $\varepsilon_d \approx 0$ and $\varepsilon_d \approx -U$. With a finite thermal bias, κ shows deviations from the linear response $T_{\rm rms}$ calculations that increase with raising the temperature gradient.

2. *The Kondo circle*

In this section, we discuss how the Kondo effect depends on the individual lead temperatures. For this, we choose the orbital level $\varepsilon_d = -U/3$, for the system to be in the local moment regime, but far enough from the particle-hole symmetry point to develop sufficient thermopower S.

Figure 4(a) presents the zero-bias differential conductance G as a function of the independent left and right lead temperatures. The conductance G has its maximum as $T_L, T_R \to 0$ and decays radially in the $T_L - T_R$ plane. In particular, we focus on the temperatures in the scaling regime, i.e. around $T = T_{\rm K}$, where the conductance $G_0(T)$ is known to exhibit universal behavior. The black [white] dashed curves denote circles of radii $\sqrt{2}\,T_{\rm K}$, where $T_{\rm K}$ is estimated from Eq. (16) [$\sqrt{2}\,T_{\rm K'}$, where $T_{\rm K'}$ is estimated as the half-width of the linear-response conductance $G_0(T_{\rm rms})$]. Though the Kondo temperature $T_{\rm K'} \approx 1.05\,T_{\rm K}$ from the numerical NRG data provides a more accurate approximation of the Kondo energy scale than the analytical formula, for the sake of generality and ease of estimation, we will stick to $T_{\rm K}$ as the definition of Kondo temperature in this paper. Therefore, the half-width of the conductance peak lying on the $T_{\rm K'}$ circle is an immediate consequence from the definition of $T_{\rm rms}$ and its correspondence to the nonlinear ΔT in the local moment regime [cf. Fig. 3(a)]. The horizontal cross-sections in panel (b) show how the conductance decays as a function of the right lead temperature T_R, where

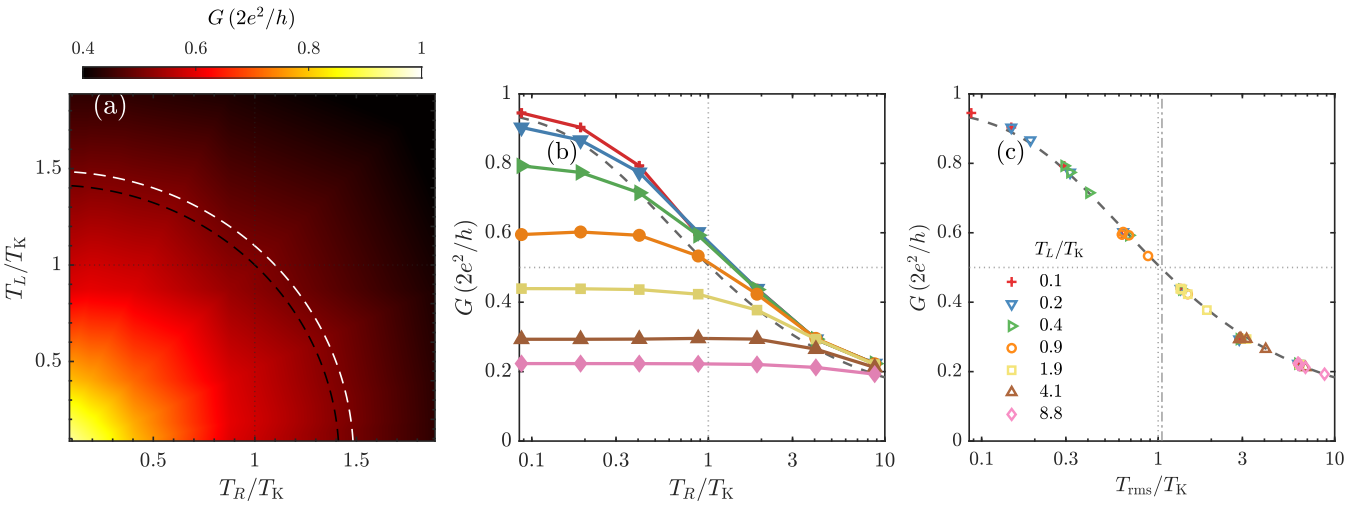

FIG. 4. (a) The differential conductance G through the quantum dot with orbital energy $\varepsilon_d = -U/3$ as in (5) as a function of the left and right lead temperatures, T_L and T_R, in the linear response regime $V \to 0$. The black dashed curve shows a circle of radius $\sqrt{2}\,T_K$ corresponding to $T_{\rm rms} = T_{\rm K}$ [cf. Eq. (16)], while the white dashed line shows $T_{\rm rms} = T_{\rm K'}$ estimated as the half-width of the zero-bias conductance peak from the NRG data versus effective temperature. The colored symbols in (b) present horizontal cross-sections of (a) for different values of T_L, as shown with panel (c) vs. T_R on a logarithmic scale. For comparison, the black dashed line displays the linear response NRG results of G vs. $T_R = T_L \equiv T$. Panel (c): Data in (b) replotted against the effective global temperature $T_{\rm rms}$ in Eq. (17). This is again contrasted with the equilibrium NRG data (black dashed line) where the vertical dash-dotted line denotes the half-width of equilibrium conductance $T_{\rm K'} \simeq 1.05\,T_{\rm K}$.

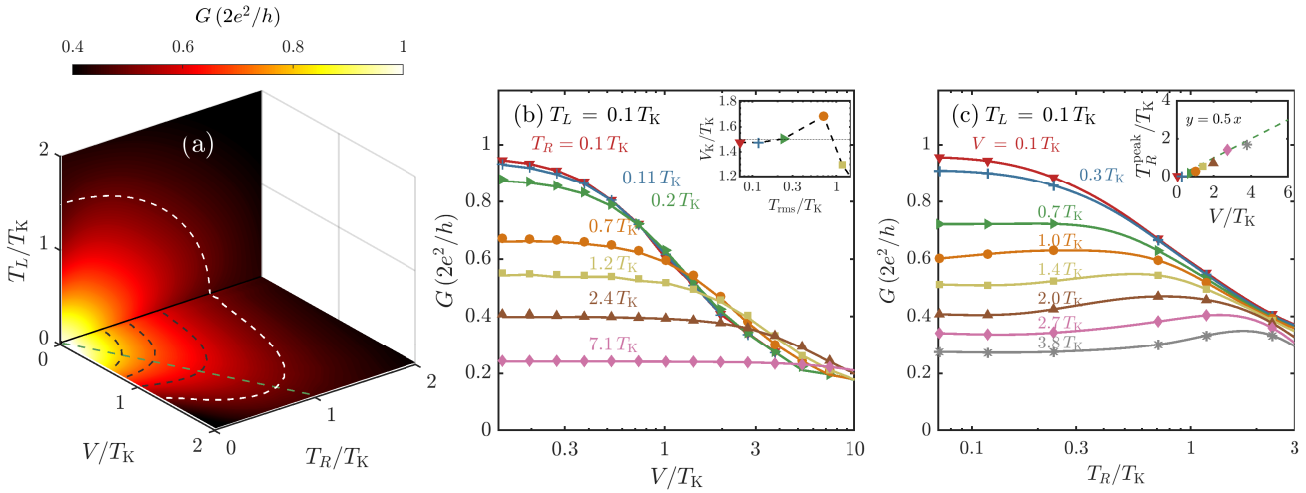

FIG. 5. (a) The differential conductance G through a quantum dot [SIAM using (5)] vs. T_L, T_R and a finite potential bias V. The data in the vertical plane is the same as in Fig. 4 (a), the horizontal plane is calculated with $T_L = 0.1\,T_{\rm K}$ and for different T_R as specified in the legends of panel (b). The black [white] dashed lines on the horizontal plane show the contours of constant conductance $G = (0.8, 0.7, 0.6)$ [$G = 0.5$]. The green dashed line indicates $T_R = V/2$, cf. inset to panel (c). Panel (b) shows the cross-sections (symbols) of the horizontal plane in panel (a) for a fixed right lead temperature as indicated by the colored labels. The solid lines show the corresponding $G(V)$ calculations for an effective global lead temperature $T_{\rm rms} = T_L = T_R$. The inset in panel (b) tracks $V_{\rm K}$, the Kondo scale in the applied bias, defined as $G(V_{\rm K}) = 0.5$. Panel (c) shows the differential conductance $G(T_R)$ from the horizontal plane in panel (a) for a finite potential difference V, as indicated by the colored labels. Lines represent spline interpolations of the semilog-x data used to estimate the peak position $T_R^{\rm peak}$. Inset shows $T_R^{\rm peak}$ vs. V, which approximately follows $T_R^{\rm peak} = V/2$ (green sdashed line).

the temperature on the left lead T_L determines the peak value of the conductance curve. The $G(T_R)$ curve lies below the linear response $G_0(T_R = T_L = T)$ curve for $T_R < T_L$ and coincides with the linear response results at $T_L = T_R$ to remain above the linear response data for $T_R > T_L$. Due to the left-right symmetry in the system, the previous arguments hold true even if one swaps T_L and T_R. The conductance data $G(T_L, T_R)$ is plotted

against the rescaled $T_{\rm rms}$ temperature in the panel (c). The rescaled data lies perfectly on top of the linear response $G_0(T_{\rm rms})$ curve. This is a useful result, especially for the experimental exploration of the Kondo regime. In experiments, where one do not reach the truly linear response regime [30–33], $T_{\rm rms}$ can provide reliable theoretical estimations from equilibrium NRG calculations to accurately identify the parameter space of the Kondo regime in T_L and T_R separately.

In general, the zero-bias conductance peak along with the Kondo resonance is known to get smeared with increasing thermal fluctuations [6, 8]. The influence of the individual lead temperatures on the whole $G(V)$ curve beyond linear response bias voltage regime is less trivial and is shown in Fig. 5(a). The lower plane in Fig. 5(a) presents the $G(V)$ calculations for a cold left lead temperature $T_L \approx 0.1\,T_{\rm K}$ and with increasing the right lead temperatures $T_R > T_L$. For small temperatures $T_R \ll T_{\rm K}$, the conductance peak remains sharp in the finite V regime but with an increase in T_R around $T_R \approx 0.2\,T_{\rm K}$ the Kondo peak starts to get smeared out in V. This behavior is clearly seen in $G(V)$ curves for different T_R presented in Fig. 5(b), where the increase in T_R suppresses the conductance at zero bias and smears the zero-bias conductance peak further into the finite V regime.

Furthermore, we observe in our simulations that any configuration of the lead temperatures $G(V)_{T_L,T_R}$ can be approximated by a $G(V)_{T_{\rm rms},T_{\rm rms}}$ curve with global temperature $T_{\rm rms}$ [cf. solid lines in Fig. 5(b)]. The Kondo energy scale in the applied bias $V_{\rm K}$, defined as the bias at which the conductance drops to one-half $G(V_{\rm K}) = 1/2$, is a characteristic energy scale of the nonequilibrium Kondo effect and behaves differently from $T_{\rm K}$. The inset in Fig. 5(b) shows the dependence of $V_{\rm K}$ on $T_{\rm rms}$. At low temperatures $T \ll T_{\rm K}$, we recover the Fermi liquid theory prediction for the Kondo energy scales $V_{\rm K}/T_{\rm K} \approx 3/2$ [64, 80, 81, 86]. It can be seen that $V_{\rm K}$ increases with $T_{\rm rms}$, corresponding to the smearing of the Kondo resonance with thermal fluctuations up to $T_{\rm rms} \approx T_{\rm K}$. Beyond which the Kondo resonance is considerably destroyed by the thermal fluctuations, such that $G(V)$ fails to attain the definition of $V_{\rm K}$ for temperatures around $T_{\rm rms} \approx 1.3\,T_{\rm K}$ [cf. Fig. 5(b)].

Figure 5(c) shows the influence of the right lead temperature T_R on the differential conductance $G(T_R)_{T_L,V}$ with a constant T_L and finite potential bias V. For very small potential biases $V \ll T_{\rm K}$, the differential conductance G monotonously decreases with increasing T_R, closely resembling the true zero-bias conductance curve in Fig. 4(b). In the case of a large potential bias $V \gtrsim T_{\rm K}$, the $G(T_R)$ curves show maxima roughly located at a finite right lead temperature $T_R^{\rm peak} \approx V/2$ [cf. inset of Fig. 5(c)]. This nonmonotonous behavior of $G(T_R)_{T_L,V}$ for $V > T_{\rm K}$ can be attributed to the splitting of the Kondo resonance in the presence of large potential biases. Due to the bias configuration in our system, $\mu_{L/R} = \pm V/2$, the peaks of the split-Kondo resonance will be located at the respective lead potentials $\mu_{L/R}$ for $V \gtrsim T_{\rm K}$, resulting in the additional feature in $G(T_R)$ around $T_R = V/2$.

3. *Thermoelectrics of the Kondo circle*

Instead of diving directly into the Seebeck coefficient, we first look at the thermoelectric current driven by the finite thermal bias in Fig. 6. The panel (a) shows the NRG-tDMRG results for the charge current as a function of both the left and right lead temperatures. The current $J(T_L,T_R)_{V=0}$ is antisymmetric across the $T_L = T_R$ line, as the temperature gradient changes sign across this line. In addition, there exists another sign change roughly as a circle in the T_L, T_R plane corresponding to the onset of Kondo correlations. The current at zero bias, computed as $J(T_L,T_R)_{V=0} = \frac{1}{2}\left(J(V_0) + J(-V_0)\right)\big|_{T_L,T_R}$ from the data for small $\pm V_0$ [cf. Eq. (13)], can be fitted by the polynomial expression up to order n as in

$$J(T_L,T_R)_{V=0} = \Gamma\,\frac{T_L-T_R}{T_{\rm rms}}\;p_n(x \equiv \tfrac{T_L}{T_{\rm K}}, y \equiv \tfrac{T_R}{T_{\rm K}}), \quad (18)$$

where

$$p_n(x,y) = \sum_{k=1}^{n}\sum_{i=0}^{k} a_{k,i}\,x^i\,y^{k-i}, \quad (19)$$

$$a_{k,i} = a_{k,k-i}\ . \quad (20)$$

Having $V = 0$, the current needs to be antisymmetric under inversion $T_L \leftrightarrow T_R$. This is taken care of by the leading factor $T_L - T_R$ on the RHS. The remaining polynomial $p_n(\frac{T_L}{T_{\rm K}}, \frac{T_R}{T_{\rm K}})$ thus must be symmetric under inversion. This constrains the polynomial terms to Eq. (20). The denominator $T_{\rm rms}$ keeps the prefactor in check for large ΔT. i.e., the ratio $\frac{T_L-T_R}{T_{\rm rms}} \to \sqrt{2}$ as $T_R \to \infty$. Thus providing a much more consistent weights for the data points with large ΔT used in the variational fitting. We note that a clean polynomial fit of the form $(T_L - T_R)\,p_n(\frac{T_L}{T_{\rm K}}, \frac{T_R}{T_{\rm K}})$ can still provide an acceptable fit for the current, but including the denominator $T_{\rm rms}$ considerably improves the fit at low T. At first glance, Eq. (18) only seems to account for the first order in ΔT. But, the first order polynomial terms T_L,T_R together with the $T_L - T_R$ prefactor makes up the $(T_L - T_R)^2 \equiv \Delta T^2$ dependence, the polynomial terms T_L^2, T_R^2 and $T_L\,T_R$ have encoded in it the information of the ΔT^3 dependence, and accordingly for the higher order dependences in ΔT. Thus the polynomial fit contains, but is not limited to, the perturbative expansion of J on ΔT.

The polynomial coefficients are determined by minimizing the cost function

$$C = \sum_i \left| J(T_L,T_R)\big|_i - \Gamma\frac{(T_L-T_R)}{T_{\rm rms}}\big|_i p_n(x_i,y_i)\right|^2, \quad (21)$$

where the sum runs over all data points i with $T_L \neq T_R$. The quality of the fit is then estimated by the error

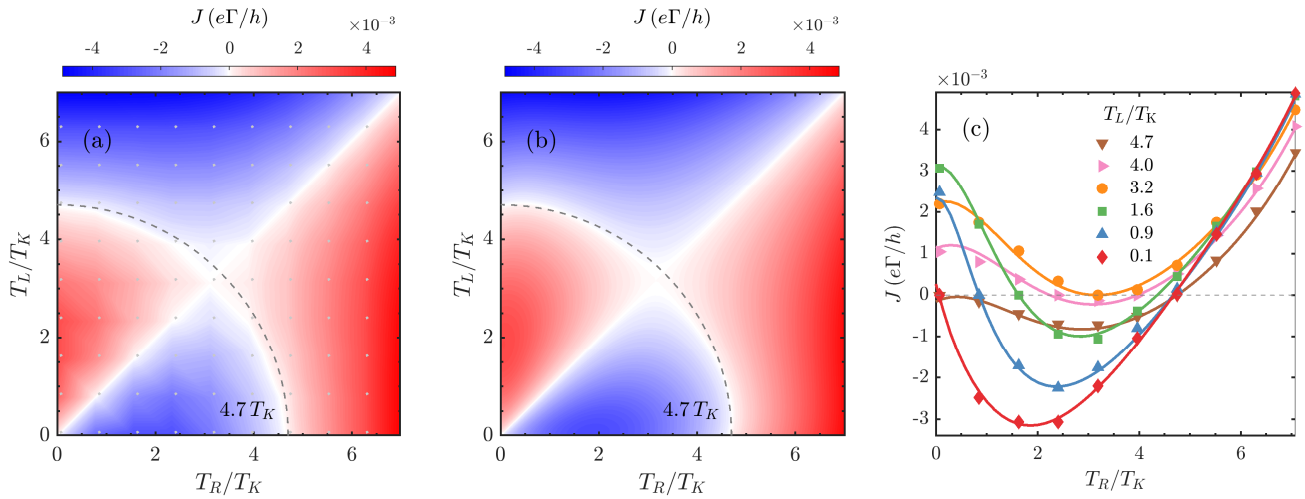

FIG. 6. (a) Thermoelectric current J through a quantum dot [SIAM using (5)] vs. T_L and T_R at $V = 0$ (computed as the average current for $V = \pm 10^{-2} T_{\mathrm{K}}$). The data points located at the white dots are interpolated by the smooth color shading (cf. color bar). Panel (b) same as panel (a), but showing the polynomial fit of its data points based on Eq. (18) instead. Panel (c) shows horizontal cuts of the polynomial fit (lines) in panel (b) with their corresponding data points (symbols) from panel (a).

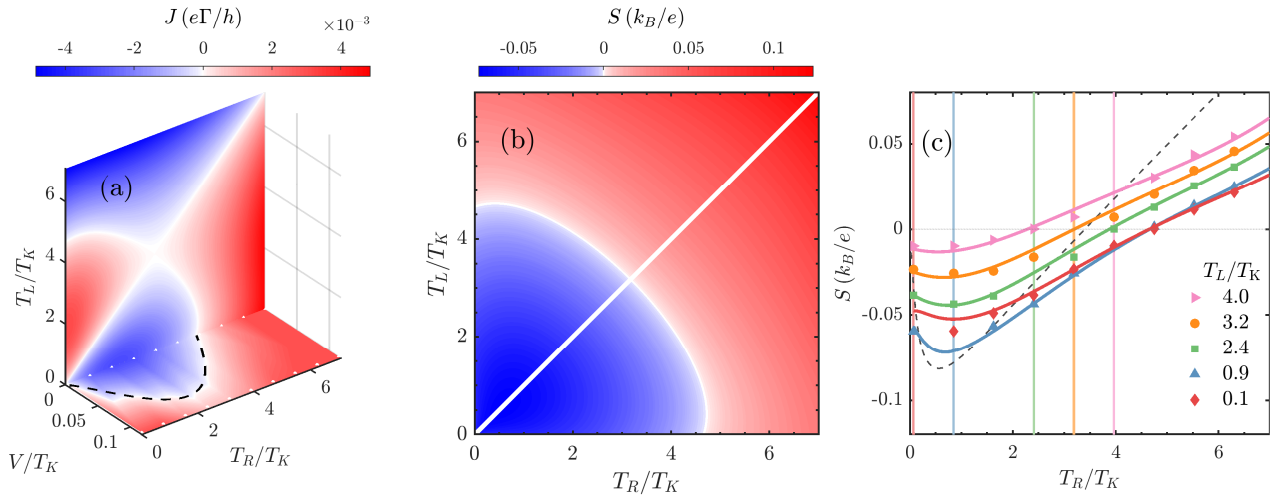

FIG. 7. (a) Thermoelectric current J through a quantum dot [SIAM using (5)] vs. T_L, T_R and for very small potential biases V. The black dashed curve shows the voltage V required to compensate the thermocurrent according to a linear response expansion with G_0. The grid of NRG-tDMRG data in V is represented as white dots on the V, T_R plane. (b) The Seebeck coefficient $S = -V/\Delta T = -J/(G\,\Delta T)$ (assuming linear response in G) for the same parameters as in panel (a). Panel (c) shows the horizontal cross-sections of the panel (b) comparing S calculated from the fit [cf. Eq. (18)] (solid line) and S estimated from $J(T_L, T_R)_{V=0}$ from NRG-tDMRG (colored symbols). For comparison, the black dashed curve shows the linear response NRG calculations for S_0 with $T_L = T_R$. The colored vertical lines denote the corresponding left lead temperature T_L for each $S(T_R)$ curve.

measure $\delta_{\mathrm{fit}} = \sqrt{\min(C)}$. The fit in Fig. 6 used $n = 4$ with coefficients

$$\begin{aligned}
(a_{10}\qquad\qquad) &= (2.7874)\\
(a_{20}, a_{21}\qquad) &= (-1.0856, -0.9690)\\
(a_{30}, a_{31}\qquad) &= (0.1363, 0.1418)\\
(a_{40}, a_{41}, a_{42}) &= (-0.0068, -0.0091, -0.0060)
\end{aligned} \tag{22}$$

The thermoelectric current from the polynomial fit Eq. (18) is shown in Figs. 6(b,c). The polynomial fit accurately recovers the regions of sign change in Fig. 6(a). The error measure of the fits presented in Table I shows that increasing order of the polynomial improves the fit quality. The fit converges at higher orders of the polynomial, indicated by the decreasing magnitude of the polynomial coefficients for the higher order terms [cf.

n	$\delta_{\rm fit}/\bar{J}$
1	0.9690
2	0.0051
3	0.0010
4	0.0002

TABLE I. The degree n of the polynomial used for the fit and corresponding error $\delta_{\rm fit}$ relative to $\bar{J}$ the largest value of thermoelectric current inside the Kondo circle.

Eq. (22)].

The estimation of S from Eq. (15) relies on the induced thermocurrent being small enough to be compensated by a linear response bias V. In Fig. 7(a) we show the extension of the density plot in Fig. 6(a) towards the third dimension in the bias voltage V. The lower plane in V, T_R is calculated for $T_L \approx 0.1\,T_{\rm K}$ [brown curve in Fig. 6(c)], which contains the largest value of thermocurrent data in the Kondo regime. The points of zero current in the lower plane show that a bias voltage $V < V_0$ is sufficient to compensate for the induced thermocurrent. The zero current (white) in the interpolated colormap from the NRG-tDMRG data for finite $V = \pm V_0$ coincides with the bias estimated from the linear response expansion (black dashed curve) of the current with the linear response conductance $G_0(T_{\rm rms})$, further corroborating the choice of the linear response V_0. Thus, Fig. 7(b) depicts the Seebeck coefficient S estimated for the full scaling regime in T_L, T_R plane. From the sign changes of the thermoelectric current $J(T_L, T_R)$ in Fig. 6, only the sign change corresponding to the Kondo correlations survive for $S(T_L, T_R)$. This region of the sign change in the Seebeck coefficient now fully represents the temperature regime in which the Kondo correlations survive. The Kondo regime is roughly a circle in the T_L, T_R plane, slightly squeezed in the $T_L = T_R$ direction. It is important to note that the radius of the Kondo regime in the T_L, T_R plane determined by the points of sign change in S does not show any universal scaling with respect to $T_{\rm K}$. The equilibrium NRG studies of S_0 have already demonstrated that the temperature at which $S_0(T)$ shows the maximum negative value in the Kondo regime scales with the Kondo temperature $T_{\rm K}$. But the temperature at which S_0 changes sign, denoting the onset of Kondo correlations, does not exhibit such scaling with respect to $T_{\rm K}$ [29].

The quantitative behavior of $S(T_L, T_R)_{V=0}$ is shown in Fig. 7(c). The Seebeck coefficient S estimated from the NRG-tDMRG calculations (colored symbols) of the thermoelectric current $J(T_L, T_R)_{V=0}$ in Fig. 6 and S estimated from the polynomial fit for the thermoelectric current (solid lines) as in Eq. (18) with a constant T_L are plotted as a function of T_R. Near the equilibrium temperature $T_R \to T_L$, the NRG-tDMRG results approach the linear response NRG estimations of S_0. We note that, since $T_L = T_R$ induces no thermoelectric current, the extraction of the linear response S_0 using NRG-tDMRG from the chosen T_L, T_R grid of discrete datapoints is not possible [cf. Eq. (15)], and hence no datapoints from NRG-tDMRG are shown for the case of $T_L = T_R$ in Fig. 7(c). The polynomial fit for the thermoelectric current from Eq. (18) is unrestrained and can provide an approximation of the linear response S_0 for $T_L \to T_R$. $S(T_R \to T_L)$ estimated from the fit shows slight quantitative difference from the true linear response S_0 obtained from NRG, presumably stemming from the absence of very small ΔT in the data used for fitting. In general, for a constant T_L in the Kondo regime, $S(T_R)$ starts from a negative value for $T_R \to 0$ and shows a minima at temperature T_R of the order of $T_{\rm K}$. With further increase in the temperature, $S(T_R)$ grows gradually until changing its sign denoting the total destruction of the Kondo resonance.

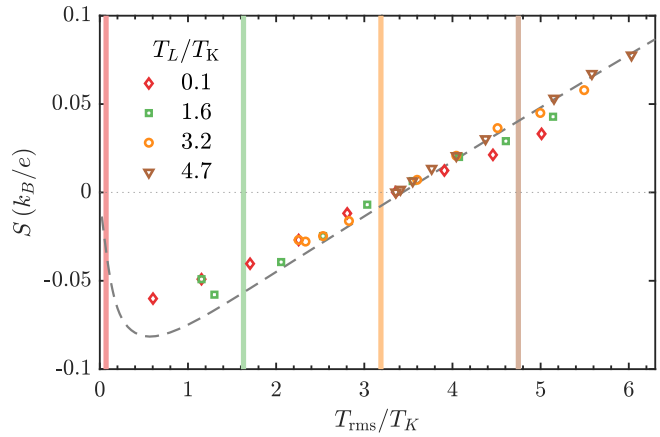

FIG. 8. The Seebeck coefficient $S\,(T_L, T_R)$ (colored symbols) with a fixed T_L (vertical colored lines) plotted against the effective temperature $T_{\rm rms}$. The dashed line shows the equilibrium NRG data for $S_0\,(T_L = T_R = T_{\rm rms})$.

The comparison of $S(T_L, T_R)$ rescaled by the effective temperature $T_{\rm rms}$ and the linear response $S_0(T)$ from NRG is presented in Fig. 8. Unlike the differential conductance $G(T_{\rm rms})$, the rescaled $S(T_{\rm rms})$ data do not fully resemble the linear response $S_0(T)$ behavior, with increasing deviations for large temperature gradients. We observe that the deviation of $S(T_{\rm rms})$ depends on the minima of the linear response S_0. We define T_p as the temperature, at which S_0 has a negative peak. When the cold lead temperature is larger than T_p, $S(T_{\rm rms})$ lies closer to the linear response S_0. But for the case of a cold lead temperature below T_p, left lead temperature $T_L \approx 0.1\,T_{\rm K}$ in our case [cf. red diamonds in Fig. 8], $S(T_{\rm rms})$ shows the largest deviations from the linear response S_0.

As an aside, let us also comment here on the so-called Mott's formula [87]

$$S_0 \approx \frac{\pi^2 k_B^2}{3\,e}\frac{T}{G_0(\mu)}\left(\frac{\partial G_0(\mu)}{\partial \mu}\right)_{\mu=E_F}. \qquad (23)$$

It holds within linear response, and relates the thermopower S_0, specifically also its sign, to the conductance G_0 and thus the behavior of the density of states near the Fermi level, with the former more readily accessible experimentally. Though one cannot directly extend Mott's formula to large temperature gradients, one can still look for qualitative insights based on it. We note that from our results, the differential conductance rescaled according to the effective temperature quantitatively resembles the linear response results [cf. Fig. 4 (c)], whereas the Seebeck coefficient shows deviations from such a scaling with respect to the effective temperature [cf. Fig. 8]. Since Mott's formula is valid for linear response thermopower of a Kondo quantum dot [29], one can state that the Mott's formula is clearly violated at large temperature gradients.

From the data in Fig. 8 we can conclude that the magnitude of the Seebeck coefficient is not enhanced when compared to linear response $S_{\rm lin}$ under zero-bias conditions even with nonlinear temperature gradients. Furthermore, the data in Fig. 8 shows rather small values $|S| \lesssim 0.1$ for the Seebeck coefficient in the Kondo regime. This is in contrast, for example, to Fig. 3 where the Seebeck coefficient can reach values an order of magnitude higher $|S| \lesssim 1$ just outside the local moment regime. Based on these findings, let us briefly comment here on how to potentially enhance the thermoelectric response in the Kondo regime [42]. It was suggested that an asymmetric coupling to the leads together with a finite potential bias can improve the thermoelectric response in the Kondo regime, as suggested in Ref. [46]. While the NRG-tDMRG method is well-suited to handle such systems, a thorough investigation of this scenario necessitates a detailed study of its own and thus is beyond the scope of the present work.

Lastly, we analyze the heat current and heat conductance in the presence of a finite temperature gradient. The heat current J^Q across the quantum dot coupled to leads with temperatures T_L and T_R is shown in Fig. 9(a). Unlike the Seebeck coefficient, there exist no sign change in the heat conductance characterizing the Kondo resonance. Thus, the heat current shows only one sign change corresponding to the change in the sign of the temperature gradient $T_L - T_R$. The electronic contribution to the heat conductance κ calculated for the cross sections in panel (a) is presented in panel (b). It can be seen that for a constant T_L, κ is enhanced with increase in T_R. When reaching $T_R = T_L$, the heat conductance smoothly crosses the linear response κ_0.

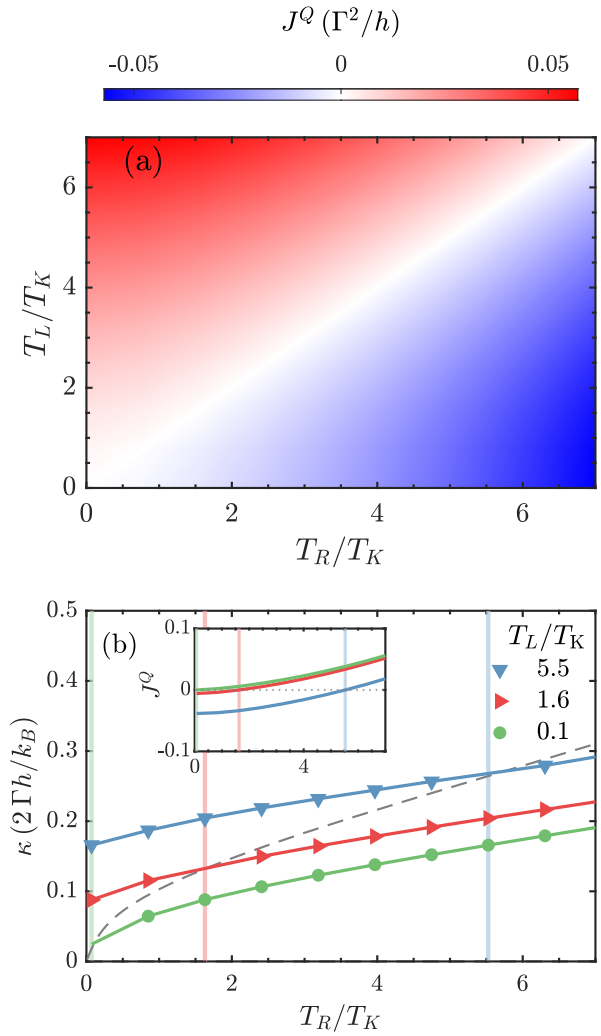

FIG. 9. (a) The heat/energy current J^Q through a quantum dot [SIAM using (5)] as a function of the left lead temperature T_L and the right lead temperature T_R. (b) shows the heat conductance κ for different values of T_L, as indicated. The dashed line corresponds to the equilibrium NRG results for $\kappa_0\,(T = T_L = T_R)$. The inset presents the horizontal cross sections of panel (a) used for the estimation of κ in panel (b).

IV. SUMMARY

In this work we have provided accurate quantitative results for the thermoelectric transport properties of a Kondo-correlated quantum dot subject to nonlinear temperature and voltage gradients. The calculations have been performed with the aid of numerical renormalization group–time-dependent density matrix renormalization group method. First of all, we have demonstrated that the thermoelectric behavior of the system, involving charge and heat currents as well as the Seebeck coefficient, can be qualitatively described by an effective global temperature $T_{\rm rms}$. Moreover, a detailed investigation of the zero-bias conductance with respect to the individual lead temperatures unveiled the Kondo regime as a circle in the plane of left-right lead temperatures, further affirming the qualitative agreement with $T_{\rm rms}$. The thermoelectric current also showed characteristic sign changes crossing over to the Kondo regime, as a slightly distorted circle with the deviations occurring at large temperature gradients. Moreover, we have pro-

vided a qualitative expression to fit the thermoelectric current as a function of the left and right lead temperatures. Finally, we have discussed the heat current and conductance near the Kondo regime, which were mostly determined by the contribution from charge fluctuations, hardly revealing characteristics of the Kondo resonance.

The thermoelectrics in the presence of finite temperature gradients at zero bias voltage did not show any enhancement of the thermoelectric properties originating from the nonlinear contributions in the Kondo regime. However, investigating the nonequilibrium regime of asymmetrically coupled Kondo-correlated systems [46] is a promising direction where NRG-tDMRG can yield reliable insights. This complex scenario warrants a dedicated study of its own which goes beyond the scope of the present work and thus is left for the future.

V. ACKNOWLEDGEMENTS

We acknowledge helpful discussions with Kacper Wrześniewski during the development of this work. This work was supported by the Polish National Science Centre from funds awarded through Decision No. NCN 2022/45/B/ST3/02826. A.M. acknowledges Brookhaven National Laboratory for hosting a research visit that contributed significantly to this work and is grateful to the NAWA-STER program for financial support provided for the visit through Decision no. PPI/STE2020/1/00007/U/00001. A.W. was supported by the U.S. Department of Energy, Office of Science, Basic Energy Sciences, Materials Sciences and Engineering Division. This work was funded in part by the Deutsche Forschungsgemeinschaft under Germany's Excellence Strategy EXC-2111 (Project No. 390814868).

VI. DATA AVAILABILITY STATEMENT

The datasets generated and analyzed for this work are publicly available on Zenodo at https://doi.org/10.5281/zenodo.13773063.

Appendix A: The Hybrid NRG-tDMRG method

We use a hybrid NRG-tDMRG method to study the nonequilibrium dynamics of the quantum dot coupled to leads with finite thermal and potential bias. Below, we provide more details about this method and its extension to finite thermal gradients.

1. Hybrid discretization scheme

Primarily, we separate the conduction band into modes that can be treated in equilibrium and out-of-equilibrium. i.e., the modes with $f_L(\omega) - f_R(\omega) = 0$ correspond to the modes that are at equilibrium and $f_L(\omega) - f_R(\omega) \neq 0$ are the modes that are out of equilibrium, where $f_\alpha(\omega)$ is the Fermi function for the lead α. For simplicity, we keep the largest $|\omega|$ that satisfies $f_L(\omega) - f_R(\omega) \neq 0$ as our effective bandwidth D^* and define the transport window as $[-D^*, D^*]$ (essentially including more equilibrium modes into the tDMRG part, which is easier to handle and provides a more accurate description than moving more nonequilibrium modes into the NRG part). The energies outside $|D^*|$ are discretized logarithmically according to the discretization parameter Λ and the energies inside $|D^*|$ are discretized linearly according to the discretization parameter δ. In this discretized setting, the coupling between the quantum dot energy level ε_d to a discretized mode in the lead α with momentum k is given as $v_q = \sqrt{\Gamma_\alpha \delta_k/\pi}$, where δ_k is the size of the corresponding interval in the discretized band.

2. Thermofield treatment

We go on to describe the modes in this log-lin discretized band under a thermofield description. This entails the introduction of an auxiliary decoupled Hilbert space akin to the physical Hilbert space. For a mode c_{q1} in the physical Hilbert space, where $q \equiv \alpha, k, \sigma$ is a composite index, we introduce an auxiliary mode c_{q2}, where the index 2 denotes that the mode is in the auxiliary Hilbert space. This enlarged Hilbert space is rotated by,

$$\begin{pmatrix} \tilde{c}_{q1} \\ \tilde{c}_{q2} \end{pmatrix} = \begin{pmatrix} \sqrt{1-f_q} & -\sqrt{f_q} \\ \sqrt{f_q} & \sqrt{1-f_q} \end{pmatrix} \begin{pmatrix} c_{q1} \\ c_{q2} \end{pmatrix}, \tag{A1}$$

such that in the rotated tilde Hilbert space, the modes $\tilde{c}_{q1}|\Omega\rangle = \tilde{c}^\dagger_{q2}|\Omega\rangle = 0$ can be interpreted as holes (1) and particles (2), where $\Omega = \prod_q (\sqrt{1-f_q}\,|0,1\rangle_q + \sqrt{f_q}\,|1,0\rangle_q)$ is a pure state that can represent the thermal expectation value of an operator A on the physical lead as $\langle A\rangle = \langle\Omega|A|\Omega\rangle$.

In the rotated Hilbert space, the lead Hamiltonian becomes,

$$\mathcal{H}_{\text{lead}} = H_{\text{lead}} + H_{\text{aux}} = \sum_{qj} \varepsilon_q c^\dagger_{qj} c_{qj} = \sum_{qj} \varepsilon_q \tilde{c}^\dagger_{qj} \tilde{c}_{qj}. \tag{A2}$$

We set $\varepsilon_{q2} = \varepsilon_{q1}$ to keep the total lead Hamiltonian $\mathcal{H}_{\text{lead}}$ diagonal. Similarly, the tunneling Hamiltonian in the rotated Hilbert space can be described as,

$$H_{\text{tun}} = \sum_{qj} (\tilde{v}_{qj} d^\dagger_{\alpha\sigma} \tilde{c}_{qj} + \text{H.c.}), \tag{A3}$$

where the couplings $\tilde{v}_{q1} = v_q\sqrt{1-f_q}$ and $\tilde{v}_{q2} = v_q\sqrt{f_q}$ become functions of the Fermi-Dirac distribution functions and, thus, encompass the information about the nonequilibrium parameters, such as the temperature and potential bias on the leads.

3. Recombination of the leads and tridiagonalization

Outside the transport window $[-D^*, D^*]$, the impurity is coupled to only half of the lead modes. Since, $f_\alpha \to 1$ results in the hole coupling $\tilde{v}_{q1} \to 0$ and $f_\alpha \to 0$ results in the particle coupling $\tilde{v}_{q2} \to 0$. This essentially means that both the high energy particle modes and the low energy hole modes decouple from the impurity. Whereas for the energies inside the transport window, we use a different approach to simplify the structure. Then, a single impurity coupled to two leads can be described using an effective model with an impurity coupled to a single recombined lead and such a recombination of the leads results in half of the modes being decoupled from the system. This results in the quantum impurity being coupled to a set of hole lead modes and another set of particle lead modes. In next step, we proceed to tridiagonalize these particle and lead modes separately, resulting in two chains that are coupled to the impurity, one from the hole modes and another from the particle modes. In these chains, we can identify two sectors, the sector from the high energy modes that lies closest to the impurity on the chain exhibiting properties of a Wilson chain, i.e., energy scale separation and couplings that decay as $t_n \sim \Lambda^{-n}$.

4. NRG treatment of high energy modes and time evolution

Since the modes outside the transport window are essentially in equilibrium, we recombine the holes and particles in the high energy sector for a more physically accurate description. This results in our impurity being coupled to an effective Wilson chain corresponding to the high energy sector, which is then further coupled to the separate hole and particle chains. We treat the recombined high energy modes using the numerical renormalization group method and extract the ground state of the high energy sector as $|\phi_{\text{ini}}\rangle$. $|\phi_{\text{ini}}\rangle$ will act as the initial state for the high energy part of the chain, where the low energy hole modes are kept empty and the particle modes filled. Thus, our initial state for the time evolution $|\psi_{\text{ini}}\rangle$ becomes

$$|\psi_{\text{ini}}\rangle = |0\rangle\otimes|0\rangle\otimes\ldots|0\rangle\otimes|\phi_{\text{ini}}\rangle\otimes|1\rangle\otimes\cdots\otimes|1\rangle\otimes|1\rangle. \quad \text{(A4)}$$

We time evolve $|\psi_{\text{ini}}\rangle$ using the second-order Trotter time evolution with a quench on the coupling between the high energy and low energy sector over a finite time window.

The NRG-tDMRG calculations for the SIAM in this paper are performed with parameters $\Lambda = 2.5$, $\delta/D^* = 0.01$, $N_{\text{keep}} = 900$ kept states in the effective NRG basis of the renormalized impurity, and a truncation tolerance of $\epsilon_{\text{SVD}} = 10^{-5}$ for the tDMRG sweeps. The observables are calculated for 100 tDMRG sweeps with the first 20 sweeps dedicated for the quench.

5. Charge and heat current

The particle current or the charge current J_α from the lead α to the quantum dot can be described as,

$$J_{\alpha\sigma} = e\,\langle \dot{N}_\sigma\rangle = -\frac{i}{\hbar}\langle [N_\sigma, H]\rangle$$

$$J_{\alpha\sigma} = \frac{e}{\hbar}\sum_k \text{Im}\left(v_{\alpha k}\,\langle d^\dagger c_{\alpha k}\rangle\right) \quad \text{(A5)}$$

$$\equiv \frac{e}{\hbar}\sum_k\sum_j \text{Im}\left(\tilde{v}_{qj}\,\langle d^\dagger \tilde{c}_{qj}\rangle\right). \quad \text{(A6)}$$

Similarly, the energy current J^E_α from the lead α to the quantum dot can be described based on the lead Hamiltonian as,

$$J^E_\alpha = \langle \dot{H}_\alpha\rangle = -\frac{i}{\hbar}\langle [H_\alpha, H]\rangle$$

$$= \frac{2e}{\hbar}\sum_{k\sigma}\sum_j \varepsilon_q \text{Im}(\tilde{v}_{qj}\langle d^\dagger \tilde{c}_{qj}\rangle). \quad \text{(A7)}$$

The symmetrized current $J_\sigma(t)$ converges faster than the individual lead currents $J_{\alpha\sigma}$,

$$J_\sigma(t) = \frac{1}{2}(J_{L\sigma}(t) - J_{R\sigma}(t)) \quad \text{(A8)}$$

Appendix B: Extracting steady state observables via linear prediction

The particle current shows a transient behavior during the quench window and starts to oscillate around a steady-state value. This steady state is extracted using linear regression. We start by generating a kernel for the oscillating part based on the training window

$$y_{n+1} = \underbrace{\begin{bmatrix} a_1 & a_2 & \cdots & a_n \end{bmatrix}}_{K} \begin{bmatrix} x_1 \\ x_2 \\ \vdots \\ x_n \end{bmatrix}, \quad \text{(B1)}$$

where the kernel K estimates the next data point y_{n+1} based on the previous n data points $\{x_1, x_2 \cdots x_n\}$. We estimate K as the least squared approximation of the data points in the training window. The spectral decomposition of the kernel has the information about the oscillating behavior of the data. In particular, we isolate the eigenvector with the real eigenvalue (corresponding to the non-oscillating part) to estimate the steady state current at $t \to \infty$

$$J(t \to \infty) = \frac{\|\vec{e}_0\|}{\sqrt{e_0}}, \quad \text{(B2)}$$

where $\vec{e}_0$ is the eigenvector corresponding to the real eigenvalue e_0. Figure 10 shows the charge current (a,b,c) and the heat current (d,e,f) dynamics of a SIAM using (5) obtained from NRG-tDMRG. The steady state value estimated from linear prediction is shown as the horizontal dashed line.

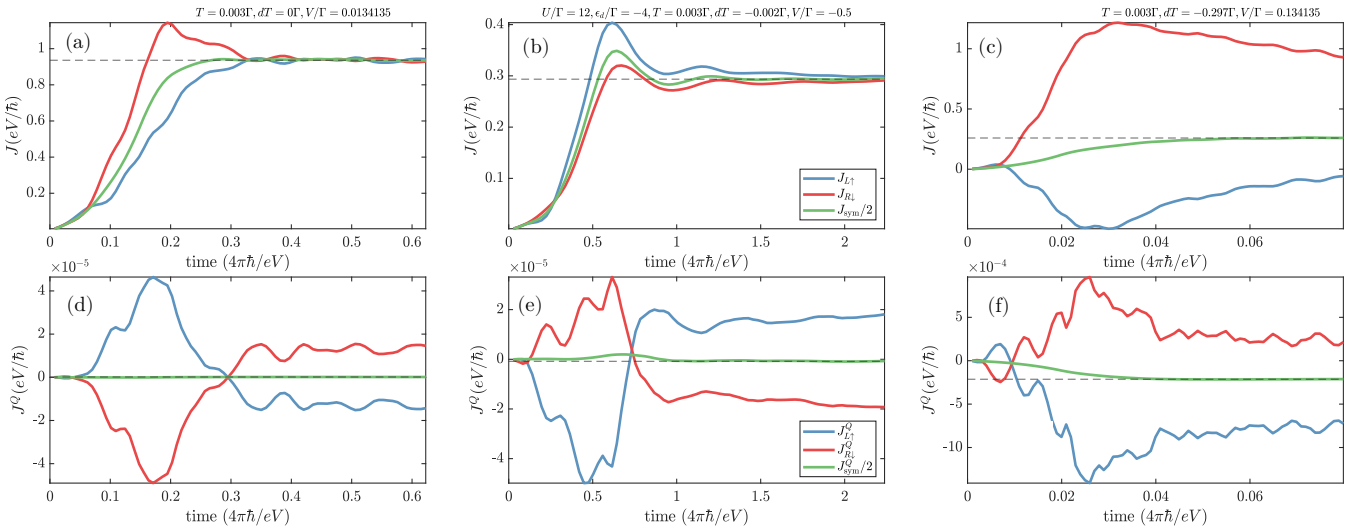

FIG. 10. The finite time dynamics of (a,b,c) charge current J and (d,e,f) heat current J^Q across a SIAM for representative values of the applied potential and temperature gradients. The horizontal dashed line shows the steady state value obtained from linear prediction.

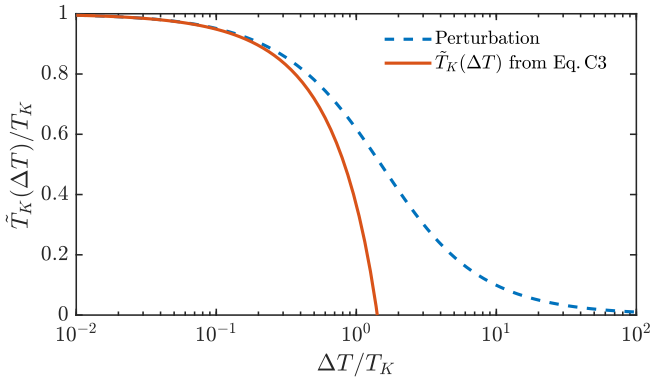

FIG. 11. The Kondo energy scale in Eq. (C3) as a function of the temperature gradient ΔT compared to the perturbation theory (Eq. (C1)) results from Ref. [60].

Appendix C: Effective Kondo energy scale

Analytical dependence of the Kondo energy scale on the temperature gradient has been discussed in Ref. [60] by using the perturbation theory and slave-boson mean-field theory. According to the perturbation theory, the Kondo energy scale depends on the temperature gradient as,

$$\tilde{T}_{\rm K}^{\rm PT}(\Delta T) = \sqrt{T_{\rm K}^2 + \left(\tfrac{\Delta T}{2}\right)^2} - \tfrac{\Delta T}{2}, \qquad \text{(C1)}$$

where $\tilde{T}_{\rm K}$ is defined as the energy scale at which the second-order term dominates in the perturbation expansion of the conductance in the Kondo model [Eq. (11) and Eq. (13) from the Ref.[60]]. Nevertheless, throughout this paper, $T_{\rm K}$ denotes the intrinsic Kondo temperature of the system as defined in Eq. (16).

From the NRG-tDMRG calculations, an effective temperature of $T_{\rm rms} = T_{\rm K}$ in the $T_L - T_R$ plane represents a circle of the form $T_L^2 + T_R^2 = 2\,T_{\rm K}^2$. To compare with the results from perturbation theory, we consider $T_L = T$ and $T_R = T + \Delta T$. Thus, we can define the energy scale $\tilde{T}_{\rm K}(\Delta T)$ for a fixed ΔT,

$$G(T, T+\Delta T)\big|_{T=\tilde{T}_{\rm K}} = G_0/2, \ , \qquad \text{(C2)}$$

i.e., as the temperature T at which $G(T, T+\Delta T)$ reaches the half maximum of the conductance peak G_0 at $T = \Delta T = 0$. By definition then, $\tilde{T}_{\rm K}$ reduces with increasing ΔT towards zero, and becomes undefined for sufficiently large $\Delta T > T_{\rm K}$ once $G(T, T+\Delta T) < G_0/2$ for all T. In this sense, $\tilde{T}_{\rm K} \to 0$ does not indicate a small physical Kondo scale, per se, but rather the disappearance of the Kondo physics. Based on the Kondo circle $T_L^2 + T_R^2 = 2\,T_{\rm K}^2$ [cf. Sec. III B 2], Eq. (C2) provides an analytical expression for $\tilde{T}_{\rm K}$

$$\tilde{T}_{\rm K}(\Delta T) = \sqrt{T_{\rm K}^2 - \left(\tfrac{\Delta T}{2}\right)^2} - \tfrac{\Delta T}{2}. \qquad \text{(C3)}$$

This expression for $\tilde{T}_{\rm K}(\Delta T)$ is very similar to the perturbation theory result, except for the difference in sign of the ΔT^2 term under the square root.

The temperature $\tilde{T}_{\rm K}$ defined on the Kondo circle and the Kondo temperature $\tilde{T}_{\rm K}^{\rm PT}$ from the perturbation theory show good agreement for small ΔT [cf. Fig. 11]. With increasing ΔT, $\tilde{T}_{\rm K}$ decays faster than $\tilde{T}_{\rm K}^{\rm PT}$ and proceed to become undefined beyond $\Delta T = \sqrt{2}\,T_K$.

[1] A. C. Hewson, The Kondo Problem to Heavy Fermions, Cambridge Studies in Magnetism (Cambridge University Press, 1993).

[2] H. Suhl, Dispersion Theory of the Kondo Effect, Phys. Rev. **138**, A515 (1965).

[3] A. A. Abrikosov and A. A. Migdal, On the theory of the Kondo effect, J. Low Temp. Phys. **3**, 519 (1970).

[4] W. J. de Haas, J. de Boer, and G. J. van dën Berg, The electrical resistance of gold, copper and lead at low temperatures, Physica **1**, 1115 (1934).

[5] D. Goldhaber-Gordon, H. Shtrikman, D. Mahalu, D. Abusch-Magder, U. Meirav, and M. A. Kastner, Kondo effect in a single-electron transistor, Nature **391**, 156 (1998).

[6] S. M. Cronenwett, T. H. Oosterkamp, and L. P. Kouwenhoven, A Tunable Kondo Effect in Quantum Dots, Science **281**, 540 (1998).

[7] J. Schmid, J. Weis, K. Eberl, and K. V. Klitzing, A quantum dot in the limit of strong coupling to reservoirs, Physica B **256-258**, 182 (1998).

[8] D. Goldhaber-Gordon, J. Göres, M. A. Kastner, H. Shtrikman, D. Mahalu, and U. Meirav, From the Kondo Regime to the Mixed-Valence Regime in a Single-Electron Transistor, Phys. Rev. Lett. **81**, 5225 (1998).

[9] F. Simmel, R. H. Blick, J. P. Kotthaus, W. Wegscheider, and M. Bichler, Anomalous Kondo Effect in a Quantum Dot at Nonzero Bias, Phys. Rev. Lett. **83**, 804 (1999).

[10] C. H. L. Quay, J. Cumings, S. J. Gamble, R. d. Picciotto, H. Kataura, and D. Goldhaber-Gordon, Magnetic field dependence of the spin-$\frac{1}{2}$ and spin-1 Kondo effects in a quantum dot, Phys. Rev. B **76**, 245311 (2007).

[11] T. S. Jespersen, M. Aagesen, C. Sørensen, P. E. Lindelof, and J. Nygård, Kondo physics in tunable semiconductor nanowire quantum dots, Phys. Rev. B **74**, 233304 (2006).

[12] S. Csonka, L. Hofstetter, F. Freitag, S. Oberholzer, C. Schönenberger, T. S. Jespersen, M. Aagesen, and J. Nygård, Giant Fluctuations and Gate Control of the g-Factor in InAs Nanowire Quantum Dots, Nano Lett. **8**, 3932 (2008).

[13] H. A. Nilsson, P. Caroff, C. Thelander, M. Larsson, J. B. Wagner, L.-E. Wernersson, L. Samuelson, and H. Q. Xu, Giant, Level-Dependent g Factors in InSb Nanowire Quantum Dots, Nano Lett. **9**, 3151 (2009).

[14] A. V. Kretinin, R. Popovitz-Biro, D. Mahalu, and H. Shtrikman, Multimode Fabry-Pérot Conductance Oscillations in Suspended Stacking-Faults-Free InAs Nanowires, Nano Lett. **10**, 3439 (2010).

[15] J. Nygård, D. H. Cobden, and P. E. Lindelof, Kondo physics in carbon nanotubes, Nature **408**, 342 (2000).

[16] A. V. Kretinin, H. Shtrikman, D. Goldhaber-Gordon, M. Hanl, A. Weichselbaum, J. von Delft, T. Costi, and D. Mahalu, Spin-$\frac{1}{2}$ Kondo effect in an InAs nanowire quantum dot: Unitary limit, conductance scaling, and Zeeman splitting, Phys. Rev. B **84**, 245316 (2011).

[17] L. H. Yu and D. Natelson, The Kondo Effect in C60 Single-Molecule Transistors, Nano Lett. **4**, 79 (2004).

[18] G. González, M. N. Leuenberger, and E. R. Mucciolo, Kondo effect in single-molecule magnet transistors, Phys. Rev. B **78**, 054445 (2008).

[19] G. D. Scott, Z. K. Keane, J. W. Ciszek, J. M. Tour, and D. Natelson, Universal scaling of nonequilibrium transport in the Kondo regime of single molecule devices, Phys. Rev. B **79**, 165413 (2009).

[20] N. Knorr, M. A. Schneider, L. Diekhöner, P. Wahl, and K. Kern, Kondo Effect of Single Co Adatoms on Cu Surfaces, Phys. Rev. Lett. **88**, 096804 (2002).

[21] M. Ternes, A. J. Heinrich, and W.-D. Schneider, Spectroscopic manifestations of the Kondo effect on single adatoms, J. Phys.: Condens. Matter **21**, 053001 (2008).

[22] J. Ren, H. Guo, J. Pan, Y. Y. Zhang, X. Wu, H.-G. Luo, S. Du, S. T. Pantelides, and H.-J. Gao, Kondo Effect of Cobalt Adatoms on a Graphene Monolayer Controlled by Substrate-Induced Ripples, Nano Lett. **14**, 4011 (2014).

[23] J.-H. Chen, L. Li, W. G. Cullen, E. D. Williams, and M. S. Fuhrer, Tunable Kondo effect in graphene with defects, Nat. Phys. **7**, 535 (2011).

[24] L. Riegger, N. Darkwah Oppong, M. Höfer, D. R. Fernandes, I. Bloch, and S. Fölling, Localized Magnetic Moments with Tunable Spin Exchange in a Gas of Ultracold Fermions, Phys. Rev. Lett. **120**, 143601 (2018).

[25] S. Seiro, L. Jiao, S. Kirchner, S. Hartmann, S. Friedemann, C. Krellner, C. Geibel, Q. Si, F. Steglich, and S. Wirth, Evolution of the Kondo lattice and non-Fermi liquid excitations in a heavy-fermion metal, Nat. Commun. **9**, 1 (2018).

[26] A. S. Shankar, D. O. Oriekhov, A. K. Mitchell, and L. Fritz, Kondo effect in twisted bilayer graphene, Phys. Rev. B **107**, 245102 (2023).

[27] C. van Efferen, J. Fischer, T. A. Costi, A. Rosch, T. Michely, and W. Jolie, Modulated Kondo screening along magnetic mirror twin boundaries in monolayer MoS2, Nat. Phys. **20**, 82 (2024).

[28] L. Kouwenhoven and L. Glazman, Revival of the Kondo effect, Phys. World **14**, 33 (2001).

[29] T. A. Costi and V. Zlatić, Thermoelectric transport through strongly correlated quantum dots, Phys. Rev. B **81**, 235127 (2010).

[30] A. Svilans, M. Josefsson, A. M. Burke, S. Fahlvik, C. Thelander, H. Linke, and M. Leijnse, Thermoelectric Characterization of the Kondo Resonance in Nanowire Quantum Dots, Phys. Rev. Lett. **121**, 206801 (2018).

[31] B. Dutta, D. Majidi, A. García Corral, P. A. Erdman, S. Florens, T. A. Costi, H. Courtois, and C. B. Winkelmann, Direct Probe of the Seebeck Coefficient in a Kondo-Correlated Single-Quantum-Dot Transistor, Nano Lett. **19**, 506 (2019).

[32] P. Gehring, J. K. Sowa, C. Hsu, J. de Bruijckere, M. van der Star, J. J. Le Roy, L. Bogani, E. M. Gauger, and H. S. J. van der Zant, Complete mapping of the thermoelectric properties of a single molecule, Nat. Nanotechnol. **16**, 426 (2021).

[33] C. Hsu, T. A. Costi, D. Vogel, C. Wegeberg, M. Mayor, H. S. J. van der Zant, and P. Gehring, Magnetic-Field Universality of the Kondo Effect Revealed by Thermocurrent Spectroscopy, Phys. Rev. Lett. **128**, 147701 (2022).

[34] L. D. Hicks and M. S. Dresselhaus, Effect of quantum-well structures on the thermoelectric figure of merit, Phys. Rev. B **47**, 12727 (1993).

[35] G. D. Mahan and J. O. Sofo, The best thermoelectric., Proc. Natl. Acad. Sci. U.S.A. **93**, 7436 (1996).

[36] J. P. Heremans, C. M. Thrush, and D. T. Morelli, Thermopower enhancement in lead telluride nanostructures,

Phys. Rev. B **70**, 115334 (2004).
[37] J. R. Szczech, J. M. Higgins, and S. Jin, Enhancement of the thermoelectric properties in nanoscale and nanostructured materials, J. Mater. Chem. **21**, 4037 (2011).
[38] J. P. Heremans, M. S. Dresselhaus, L. E. Bell, and D. T. Morelli, When thermoelectrics reached the nanoscale, Nat. Nanotechnol. **8**, 471 (2013).
[39] S. Hershfield, K. A. Muttalib, and B. J. Nartowt, Nonlinear thermoelectric transport: A class of nanodevices for high efficiency and large power output, Phys. Rev. B **88**, 085426 (2013).
[40] D. Sánchez and H. Linke, Focus on thermoelectric effects in nanostructures, New J. Phys. **16**, 110201 (2014).
[41] G. Benenti, G. Casati, K. Saito, and R. S. Whitney, Fundamental aspects of steady-state conversion of heat to work at the nanoscale, Phys. Rep. **694**, 1 (2017).
[42] D. Sánchez and R. López, Nonlinear phenomena in quantum thermoelectrics and heat, C. R. Phys. **17**, 1060 (2016).
[43] S. Andergassen, T. A. Costi, and V. Zlatić, Mechanism for large thermoelectric power in molecular quantum dots described by the negative-U Anderson model, Phys. Rev. B **84**, 241107 (2011).
[44] G. Gómez-Silva, P. A. Orellana, and E. V. Anda, Enhancement of the thermoelectric efficiency in a T-shaped quantum dot system in the linear and nonlinear regimes, J. Appl. Phys. **123**, 085706 (2018).
[45] R. Santiago Cortes-Santamaria, J. A. Landazabal-Rodríguez, J. Silva-Valencia, E. Ramos, M. S. Figueira, and R. Franco Peñaloza, Universality and the thermoelectric transport properties of a double quantum dot system: Seeking for conditions that improve the thermoelectric efficiency, SciPost Phys. Core **7**, 058 (2024).
[46] D. Pérez Daroca, P. Roura-Bas, and A. A. Aligia, Enhancing the nonlinear thermoelectric response of a correlated quantum dot in the Kondo regime by asymmetrical coupling to the leads, Phys. Rev. B **97**, 165433 (2018).
[47] A. Manaparambil and I. Weymann, Nonequilibrium Seebeck effect and thermoelectric efficiency of Kondo-correlated molecular junctions, Phys. Rev. B **107**, 085404 (2023).
[48] A. Dorda, M. Ganahl, S. Andergassen, W. von der Linden, and E. Arrigoni, Thermoelectric response of a correlated impurity in the nonequilibrium Kondo regime, Phys. Rev. B **94**, 245125 (2016).
[49] F. Giazotto, T. T. Heikkilä, A. Luukanen, A. M. Savin, and J. P. Pekola, Opportunities for mesoscopics in thermometry and refrigeration: Physics and applications, Rev. Mod. Phys. **78**, 217 (2006).
[50] S.-Y. Hwang, B. Sothmann, and D. Sánchez, Superconductor–quantum dot hybrid coolers, Phys. Rev. B **107**, 245412 (2023).
[51] X. Zeng, D. Zhang, L. Ye, L. Cao, R.-X. Xu, X. Zheng, and M. Di Ventra, Kondo cooling in quantum impurity systems, Phys. Rev. B **109**, 115423 (2024).
[52] N. Andrei, K. Furuya, and J. H. Lowenstein, Solution of the Kondo problem, Rev. Mod. Phys. **55**, 331 (1983).
[53] P. B. Wiegmann, Exact solution of the s-d exchange model (Kondo problem), J. Phys. C: Solid State Phys. **14**, 1463 (1981).
[54] P. W. Anderson, A poor man's derivation of scaling laws for the Kondo problem, J. Phys. C: Solid State Phys. **3**, 2436 (1970).
[55] P. Nozières, A "fermi-liquid" description of the Kondo problem at low temperatures, J. Low Temp. Phys. **17**, 31 (1974).
[56] A. Georges, G. Kotliar, W. Krauth, and M. J. Rozenberg, Dynamical mean-field theory of strongly correlated fermion systems and the limit of infinite dimensions, Rev. Mod. Phys. **68**, 13 (1996).
[57] K. G. Wilson, The renormalization group: Critical phenomena and the Kondo problem, Rev. Mod. Phys. **47**, 773 (1975).
[58] R. Bulla, T. A. Costi, and T. Pruschke, Numerical renormalization group method for quantum impurity systems, Rev. Mod. Phys. **80**, 395 (2008).
[59] R. Van Roermund, S.-y. Shiau, and M. Lavagna, Anderson model out of equilibrium: Decoherence effects in transport through a quantum dot, Phys. Rev. B **81**, 165115 (2010).
[60] M. A. Sierra, R. López, and D. Sánchez, Fate of the spin-$\frac{1}{2}$ Kondo effect in the presence of temperature gradients, Phys. Rev. B **96**, 085416 (2017).
[61] U. Eckern and K. I. Wysokiński, Two- and three-terminal far-from-equilibrium thermoelectric nano-devices in the Kondo regime, New J. Phys. **22**, 013045 (2020).
[62] A. Kaminski, Yu. V. Nazarov, and L. I. Glazman, Universality of the Kondo effect in a quantum dot out of equilibrium, Phys. Rev. B **62**, 8154 (2000).
[63] A. Oguri, Fermi-liquid theory for the Anderson model out of equilibrium, Phys. Rev. B **64**, 153305 (2001).
[64] C. Mora, C. P. Moca, J. von Delft, and G. Zaránd, Fermi-liquid theory for the single-impurity Anderson model, Phys. Rev. B **92**, 075120 (2015).
[65] A. Oguri and A. C. Hewson, Higher-order Fermi-liquid corrections for an Anderson impurity away from half filling: Nonequilibrium transport, Phys. Rev. B **97**, 035435 (2018).
[66] Y. Teratani, K. Tsutsumi, K. Motoyama, R. Sakano, and A. Oguri, Thermoelectric transport and current noise through a multilevel Anderson impurity: Three-body Fermi-liquid corrections in quantum dots and magnetic alloys, arXiv 10.48550/arXiv.2404.05947 (2024), 2404.05947.
[67] S. Csonka, I. Weymann, and G. Zarand, An electrically controlled quantum dot based spin current injector, Nanoscale **4**, 3635 (2012).
[68] D. M. Fugger, A. Dorda, F. Schwarz, J. von Delft, and E. Arrigoni, Nonequilibrium Kondo effect in a magnetic field: auxiliary master equation approach, New J. Phys. **20**, 013030 (2018).
[69] D. M. Fugger, D. Bauernfeind, M. E. Sorantin, and E. Arrigoni, Nonequilibrium pseudogap Anderson impurity model: A master equation tensor network approach, Phys. Rev. B **101**, 165132 (2020).
[70] N. S. Wingreen and Y. Meir, Anderson model out of equilibrium: Noncrossing-approximation approach to transport through a quantum dot, Phys. Rev. B **49**, 11040 (1994).
[71] M. H. Hettler, J. Kroha, and S. Hershfield, Nonequilibrium dynamics of the Anderson impurity model, Phys. Rev. B **58**, 5649 (1998).
[72] Th. Pruschke, R. Gezzi, and V. Meden, Non-equilibrium properties of mesoscopic systems – functional renormalization group approach, Phys. Status Solidi B **244**, 2384 (2007).
[73] J. Eckel, F. Heidrich-Meisner, S. G. Jakobs, M. Thorwart, M. Pletyukhov, and R. Egger, Comparative study

of theoretical methods for non-equilibrium quantum transport, New J. Phys. **12**, 043042 (2010).

[74] M. Pletyukhov and H. Schoeller, Nonequilibrium Kondo model: Crossover from weak to strong coupling, Phys. Rev. Lett. **108**, 260601 (2012).

[75] F. Heidrich-Meisner, A. E. Feiguin, and E. Dagotto, Real-time simulations of nonequilibrium transport in the single-impurity Anderson model, Phys. Rev. B **79**, 235336 (2009).

[76] P. Werner, T. Oka, and A. J. Millis, Diagrammatic Monte Carlo simulation of nonequilibrium systems, Phys. Rev. B **79**, 035320 (2009).

[77] E. Gull, D. R. Reichman, and A. J. Millis, Numerically exact long-time behavior of nonequilibrium quantum impurity models, Phys. Rev. B **84**, 085134 (2011).

[78] A. Koga, Quantum Monte Carlo study of nonequilibrium transport through a quantum dot coupled to normal and superconducting leads, Phys. Rev. B **87**, 115409 (2013).

[79] S. Weiss, J. Eckel, M. Thorwart, and R. Egger, Iterative real-time path integral approach to nonequilibrium quantum transport, Phys. Rev. B **77**, 195316 (2008).

[80] F. Schwarz, I. Weymann, J. von Delft, and A. Weichselbaum, Nonequilibrium Steady-State Transport in Quantum Impurity Models: A Thermofield and Quantum Quench Approach Using Matrix Product States, Phys. Rev. Lett. **121**, 137702 (2018).

[81] A. Manaparambil, A. Weichselbaum, J. von Delft, and I. Weymann, Nonequilibrium spintronic transport through Kondo impurities, Phys. Rev. B **106**, 125413 (2022).

[82] H. Haug and A.-P. Jauho, Quantum Kinetics in Transport and Optics of Semiconductors (Springer, Berlin, Germany).

[83] A. Weichselbaum, Non-abelian symmetries in tensor networks: A quantum symmetry space approach, Ann. Phys. **327**, 2972 (2012).

[84] A. Weichselbaum, X-symbols for non-Abelian symmetries in tensor networks, Phys. Rev. Res. **2**, 023385 (2020).

[85] A. Weichselbaum, QSpace - An open-source tensor library for Abelian and non-Abelian symmetries, arXiv 10.48550/arXiv.2405.06632 (2024), 2405.06632.

[86] M. Filippone, C. P. Moca, A. Weichselbaum, J. von Delft, and C. Mora, At which magnetic field, exactly, does the Kondo resonance begin to split? A Fermi liquid description of the low-energy properties of the Anderson model, Phys. Rev. B **98**, 075404 (2018).

[87] N. F. Mott and H. Jones, The Theory of the Properties of Metals and Alloys (Dover Publications Inc., Mineola, NY, USA, 1958).